ELSEVIER

Volume 182, Number 2, February 2009

JOURNAL OF SOLID STATE CHEMISTRY

www.elsevier.com/locate/jssc

CONTENTS

Abstracted/indexed in BioEngineering Abstracts, Chemical Abstracts, Coal Abstracts, Current Contents/Physics, Chemical, & Earth Sciences, Engineering Index, Research Alert, SCISEARCH, Science Abstracts, and Science Citation Index. Also covered in the abstract and citation database SCOPUS®. Full text available on ScienceDirect®.

Regular Articles

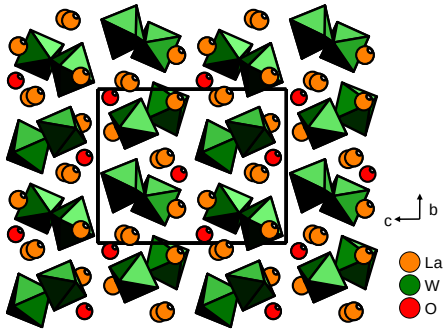

Projection of La_2WO_6 structure along [100]. The structure could be described by $[W_2O_{11}]^{-10}$ structural unit formed by two corner-sharing octahedra.

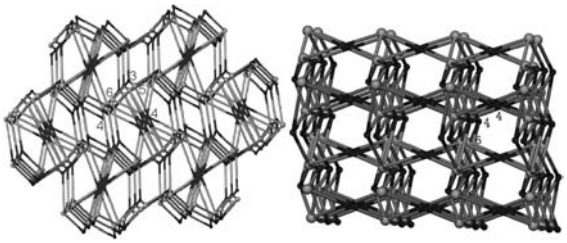

Three lanthanide–organic frameworks have been synthesized under hydrothermal conditions. Compound **1** presents a very complicated net with five types of nodes comprising intersecting (3,4)-connected and $CdSO_4$ nets. Compound **2** possesses a (4,4,6)-connected net with $(4^28^4)(4^46^2)_2(4^96^6)_2$ circuit symbol while compound **3** is a 2D layer based upon carboxylate-bridged La^{III} chains.

Regular Articles—Continued

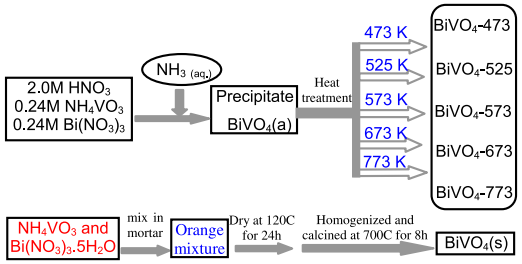

$BiVO_4$ was prepared by a co-precipitation process using aqueous ammonia solution, followed by heating treatment at various temperatures. The crystalline structure and crystallization process, and their influences on photocatalytic O_2 evolution and organic pollutants degradation were investigated. It demonstrated that the crystalline structure is still the vital factor for the activities of both reactions. However, the crystallinity of $BiVO_4$ gives a major influence on the activity of O_2 evolution, whereas the surface area, plays an important role for photocatalytic MB decomposition.

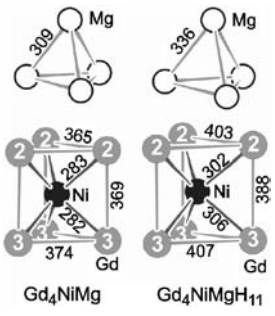

The Mg_4 and $NiGd_6$ units in Gd_4NiMg and Gd_4NiMgH_x.

Continued

Morphology modulated growth of bismuth tungsten oxide nanocrystals

Shushan Yao, Jiyong Wei, Baibiao Huang, Shengyu Feng, Xiaoyang Zhang, Xiaoyan Qin, Peng Wang, Zeyan Wang, Qi Zhang, Xiangyang Jing and Jie Zhan

Page 236

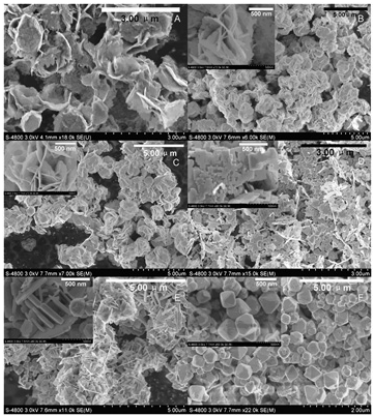

The morphology modulation of bismuth tungsten oxide nanocrystals synthesized by microwave hydrothermal method with precursor suspension's pH varied from 0.25 (strong acid) to 10.05 (base) was studied. The 3D flower like aggregation of Bi_2WO_6 nanoflakes and nanooctahedron crystals of $Bi_{3.84}W_{0.16}O_{6.24}$ were prepared. The growth mechanisms of Bi_2WO_6 and $Bi_{3.84}W_{0.16}O_{6.24}$ were attributed to the different precipitation ability and solubility of H_2WO_4 and $Bi(OH)_3$ in precursor suspensions with various pH. The photocatalytic evaluation, via the decomposition of Rhodamine B (RhB) under visible light irradiation ($\lambda > 420$ nm), reveals that nanocrystalline Bi_2WO_6 samples obtained in different condition exhibit different photocatalytic activities which depend on pH value of the precursor suspensions.

Structure and high-temperature thermoelectric properties of $SrAl_2Si_2$

Susan M. Kauzlarich, Cathie L. Condron, Jonathan K. Wassei, Teruyuki Ikeda and G. Jeffrey Snyder

Page 240

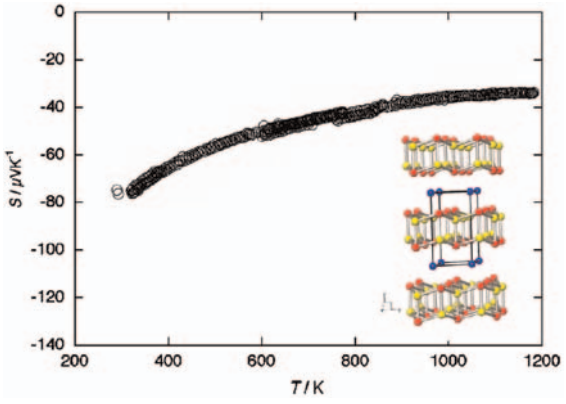

Single crystals of $SrAl_2Si_2$ have been prepared via an Al flux reaction and are of the $CaAl_2Si_2$ structure type. The melting point is approximately 1020°C. Low temperature resistivity curve is similar to that observed for single crystals of $CaAl_2Si_2$ High temperature Seebeck coefficient is negative, indicating n-type carriers.

Enhanced quantum yield of yellow photoluminescence of Dy^{3+} ions in nonlinear optical $Ba_2TiSi_2O_8$ nanocrystals formed in glass

N. Maruyama, T. Honma and T. Komatsu

Page 246

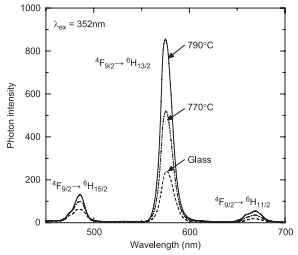

This figure shows the photoluminescence spectra of Dy^{3+} ions in the range of 450–700 nm obtained in the quantum field measurements for the precursor BTS and crystallized (at 770 and 790 °C, for 30 min) glasses. The wavelength of the excitation light was 352 nm. By incorporating into $Ba_2TiSi_2O_8$ nanocrystals, the emission intensity of the yellow band of Dy^{3+} ions is largely enhanced. This would give an impact in the science and technology of photoluminescence materials.

Magnetic properties of $KNaMSi_4O_{10}$ compounds (M=Mn, Fe, Cu)

P. Brandão, J. Rocha, M.S. Reis, A.M. dos Santos and R. Jin

Page 253

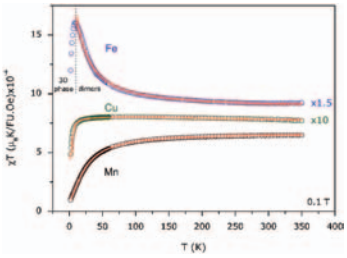

Magnetic susceptibility times temperature. The antiferromagnetic arrangement within Mn and Cu dimers is evident (due to the positive derivative at lower temperatures). For the Fe-counterpart a three-dimensional transition to an antiferromagnetic (AF) inter-dimer interaction is found upon cooling. Above this transition the drop in χT is a signature of ferromagnetic intra-dimer interactions.

Solvothermal crystal growth of $CuSbQ_2$ (Q=S, Se) and the correlation between macroscopic morphology and microscopic structure

Jian Zhou, Guo-Qing Bian, Qin-Yu Zhu, Yong Zhang, Chun-Ying Li and Jie Dai

Page 259

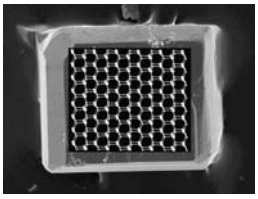

Two isostructural compounds, $CuSbQ_2$ (Q=S, Se), display different morphologies in crystals, which is explained by comparing the strength of the interlayer interactions based on the crystal structure data.

Structure and magnetic properties of RE_2Cu_2Cd
Falko M. Schappacher, Wilfried Hermes and Rainer Pöttgen
Page 265

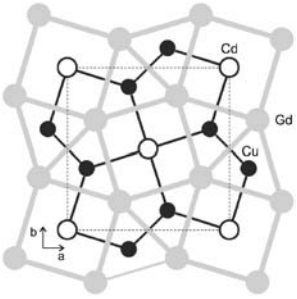

The intergrowth structure of Gd_2Cu_2Cd.

Structural and magnetic properties of the quaternary oxides $Ba_6Ln_2Fe_4O_{15}$ (Ln = Pr and Nd)
Kyosuke Abe, Yoshihiro Doi, Yukio Hinatsu and Kenji Ohoyama
Page 273

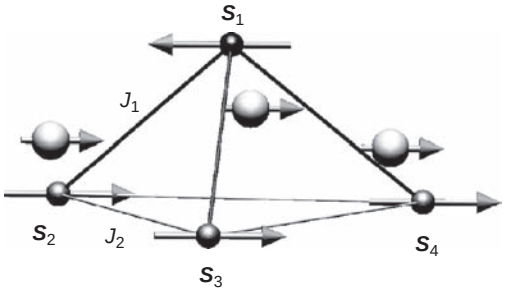

Quaternary oxides $Ba_6Ln_2Fe_4O_{15}$ (Ln = Pr and Nd) have the $Ba_6Nd_2Al_4O_{15}$-type structure with space group $P6_3mc$. In them, the magnetic moments for the ferrimagnetic Fe_4O_{15} cluster (smaller circles: Fe^{3+} ions) and Ln^{3+} ions (larger ones) cooperatively show an antiferromagnetic ordering at low temperatures.

Crystal structure and magnetic properties of high-oxygen pressure annealed $Sr_{1-x}La_xCo_{0.5}Fe_{0.5}O_{3-\delta}$ ($0 \leqslant x \leqslant 0.5$)
Konrad Świerczek, Bogdan Dabrowski, Leopoldo Suescun and Stanislaw Kolesnik
Page 280

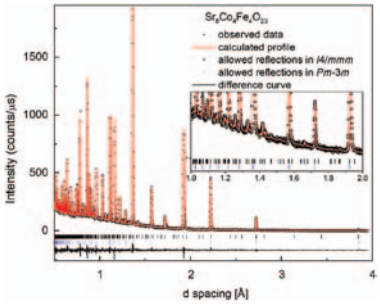

Room temperature Rietveld refinement profile using $I4/mmm$ space group for the oxygen vacancy ordered $SrCo_{0.5}Fe_{0.5}O_{2.89}$ ($Sr_8Co_4Fe_4O_{23}$). Top tick-marks denote allowed reflections in $I4/mmm$, bottom one emphasize the possibility of inexact indexing using $Pm\bar{3}m$ symmetry. Previous reports indicate that similar ordering is common for $SrCo_{1-x}Fe_xO_{3-\delta}$ compounds possibly hindering their applications.

Local environment in $Ba_2In_{2-x}W_xO_{5+3x/2}$ oxide ion conductors
Sylvie Daviero-Minaud, Aurélie Rolle, Chanapa Kongmark and Rose-Noëlle Vannier
Page 289

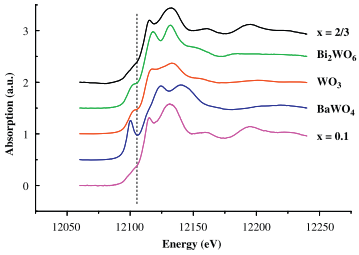

Evolution of the XANES signal of $Ba_2In_{2-x}W_xO_{5+x}$ type compounds with $x = 0.1$ (orthorhombic), $x = 2/3$ (cubic) and of $BaWO_4$, Bi_2WO_6 and WO_3 references, in which tungsten has, respectively, a tetrahedral, distorted octahedral and quasi-regular octahedral environment.Text3.

Crystal growth of a series of lithium garnets $Ln_3Li_5Ta_2O_{12}$ (Ln = La, Pr, Nd): Structural properties, Alexandrite effect and unusual ionic conductivity
Irina P. Roof, Mark D. Smith, Edmund J. Cussen and Hans-Conrad zur Loye
Page 295

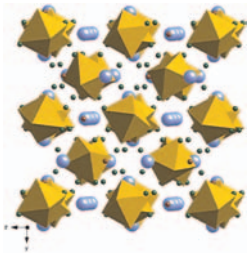

Crystal structure of garnets $Ln_3Li_5Ta_2O_{12}$ (Ln = La, Pr, Nd). TaO_6 polyhedra are shown in yellow and Ln^{3+} are shown as light blue spheres. Octahedrally and tetrahedrally coordinated Li^+ ions are shown in green and brown, respectively. Oxygen atoms are omitted for clarity.

Crystal, electronic structures and photoluminescence properties of rare-earth doped $LiSi_2N_3$
Y.Q. Li, N. Hirosaki, R.J. Xie, T. Takeka and M. Mitomo
Page 301

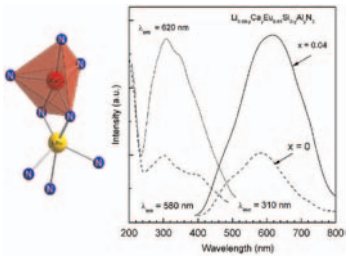

Local crystal structure and luminescence spectra of $Li_{1-2x-y}Ca_yEu_xSi_{2-y}Al_yN_3$. The emission band of Eu^{2+} shifts from yellow to red spectral region by the double substitution $Ca^{2+} \rightarrow Li^+$ and $Al^{3+} \rightarrow Si^{4+}$ simultaneously in $Li_{1-2x}Eu_xSi_2N_3$ due to the significant changes in the local environment of the $Li_{Ca,\ Eu}$ ions.

Continued

Preparation of porous TiO_2/silica composites without any surfactants

Suxia Ren, Xu Zhao, Lina Zhao, Meirong Yuan, Yang Yu, Yupeng Guo and Zichen Wang

Page 312

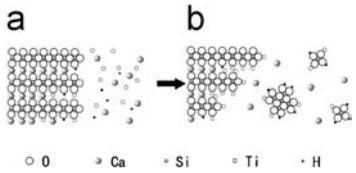

TiO_2–SiO_2 composites have been synthesized from wollastonite and titanium sulfate in the absence of any surfactants. In acid $Ti(SO_4)_2$ solution, Ca and Si ions in chain-like wollastonite could dissolve into the bulk solution and slightly soluble $CaSO_4$ crystal phase and silicic acid formed. The concentration of the titanium species in the reaction solution is expected to increase with the hydrolysis process, nucleation starts. After the start of the nucleation, a very small amount of TiO_2, silicate and $CaSO_4$ particle deposited together and formed composites. Some cavities formed during the washing step through the dissolution of $CaSO_4$ crystal phase. The bulk of the material is then transformed from wollastonite into TiO_2/silica composites.

Phase transition in the Ruddlesden–Popper layered perovskite $Li_2SrTa_2O_7$

T. Pagnier, N. Rosman, C. Galven, E. Suard, J.L. Fourquet, F. Le Berre and M.P. Crosnier-Lopez

Page 317

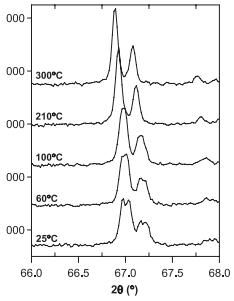

Thermal evolution of $Li_2SrTa_2O_7$ X-ray powder diffraction patterns showing the structural transformation from orthorhombic to tetragonal cell.

Structural and physical properties of 1:2 *B*-site-ordered perovskite $Ba_3CaIr_2O_9$

J.G. Zhao, L.X. Yang, Y. Yu, F.Y. Li, R.C. Yu and C.Q. Jin

Page 327

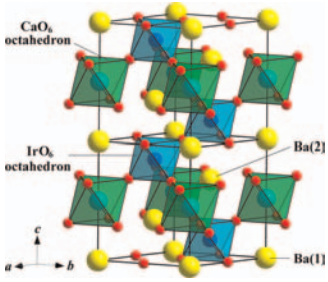

The high-pressure form of iridium-based perovskite $Ba_3CaIr_2O_9$ crystals into the 1:2 *B*-site-ordered perovskite-type structure, with the ordered arrangement of Ca and Ir ions in *B*-site.

Crystal structure and magnetic properties of the solid-solution phase $Ca_3Co_{2-v}Mn_vO_6$

C.H. Hervoches, H. Okamoto, A. Kjekshus, H. Fjellvåg and B.C. Hauback

Page 331

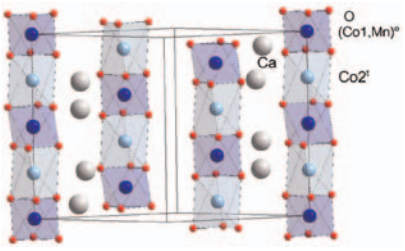

Diagonal cut through the rhombohedral crystal structure of $Ca_3Co_{2-v}Mn_vO_6$ (crystallographic formula, $Ca_3Co1_{1-v}Mn_vCo2O_6$) with emphasis on its characteristic one-dimensional columnar traits. Magnetic moments on the transition metal sites order parallel to [001] below ~25/18 K. For $0 \leqslant v < \sim 0.3$ the state is referred to as ferrimagnetic although this designation becomes increasingly approximative as v increases. For $\sim 0.5 < v < \sim 1$ an antiferromagnetic state is adopted in which the magnetic moments on both magnetic sublattices order antiferromagnetically.

Facile sonochemical synthesis and photoluminescent properties of lanthanide orthophosphate nanoparticles

Cuicui Yu, Min Yu, Chunxia Li, Xiaoming Liu, Jun Yang, Piaoping Yang and Jun Lin

Page 339

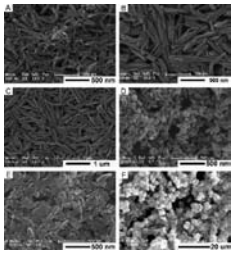

Hexagonal $LnPO_4$ (Ln = La, Ce, Pr, Nd, Sm, Eu, Gd) and tetragonal $LnPO_4$ (Ln = Tb, Dy, Ho) nanoparticles have been synthesized by a simple and facile sonochemical method.

Structured diffuse scattering and the fundamental 1-d dipolar unit in PLZT $(Pb_{1-y}La_y)_{1-\alpha}(Zr_{1-x}Ti_x)_{1-\beta}O_3$ (7.5/65/35 and 7.0/60/40) transparent ferroelectric ceramics

Ray L. Withers, Yun Liu and T.R. Welberry

Page 348

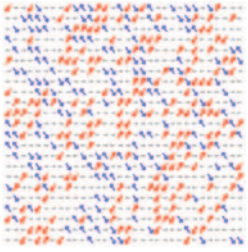

Shows a plausible model for the nano-scale polar ordering of the PLZT (7.5/65/35 and 7.0/60/40) transparent ferroelectric samples in a single layer of the average cubic structure normal to a [110] direction. The fundamental dipolar units in these materials correspond to highly anisotropic ⟨111⟩ chain dipoles formed from off-centre Pb and coupled Ti/Zr displacements.

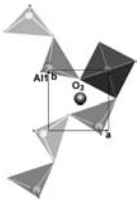

In contrast to $Sr_2Al_{1.07}Mn_{0.93}O_5$, the local atomic arrangement in these layers consist of short fragments of brownmillerite-type tetrahedral chains of corner-sharing AlO_4 tetrahedra interrupted by MnO_6 octahedra, at which the chain fragments rotate over 90°. When derived by bulk structure determination techniques such as X-ray powder diffraction, the structure will be described with an averaged tetragonal symmetry.

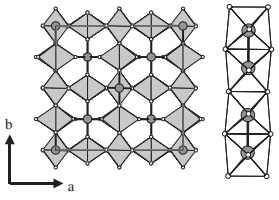

Complex rhenium oxides MRe_2O_6 crystallize in different rutile-like polymorphs depending on synthesis temperature. Low temperature modifications contain chains of edge-sharing ReO_6-octahedra with Re–Re bonds.

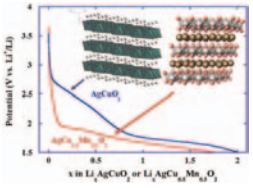

Investigation on the transport properties of $AgCuO_2$ and the new B-site mixed Delafossite $AgCu_{0.5}Mn_{0.5}O_2$ shows a p-type conductivity of $\sigma = 3.2 \times 10^{-1}$ and 1.8×10^{-4} S/cm, respectively. The high conductivity, as a result from a high charge carrier density in $AgCuO_2$ supports the existence of a mixed valence state between silver and copper. A particular emphasis is also placed on the electrochemical lithium insertion properties into these two materials by in situ XRD measurements to better insight on the Li^+ insertion mechanism and also scrutinize possible new compounds electrochemically accessible in the Li–Ag–Cu system.

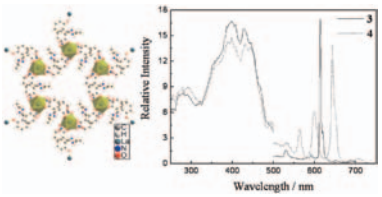

Five coordination polymers were synthesized. Given is the perspective view of a H_2L bridged hexametal ring along the c axis for **2** (La), excitation and emission spectra of **3** (Eu) and **4** (Sm) in the solid state.

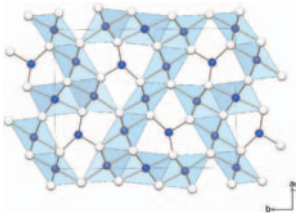

$MgAl_2O_4$ dissociates into a mixture of Al_2O_3 corundum and a new high-pressure phase of $Mg_2Al_2O_5$ at high pressures and temperatures. The $Mg_2Al_2O_5$ phase represents a new structure type with orthorhombic symmetry, showing the projection to (0 0 1) plane. The structure consists of edge- and corner-shared (Mg, Al)O_6 octahedra, and contains chains of edge-shared octahedra running along the c-axis.

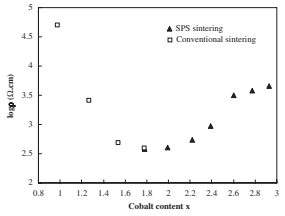

After elaboration of single-phase and well densified ceramics $Mn_{3-x}Co_xO_4$ (with $0.98 \leqslant x \leqslant 3$) by conventional and spark plasma sintering, electrical measurements have been taken and low values of resistivity can be achieved. The conductivity shifts from an insulator, Mn_3O_4 (cationic distribution: $Mn^{2+}[Mn^{3+}]_2O_4$) to a semiconductor solid solution probably due to the hopping of polarons between Mn^{3+} and Mn^{4+} on octahedral sites.

Continued

Syntheses, structures, characterizations and charge-density matching of novel amino-templated uranyl selenates
Jie Ling, Ginger E. Sigmon and Peter C. Burns
Page 402

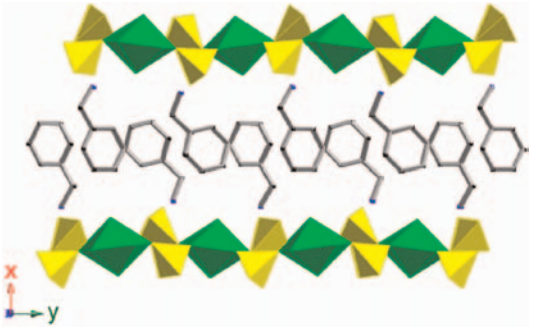

The structures of five new inorganic–organic hybrid uranyl selenates present new structural topologies based upon chains and sheets of uranyl pentagonal bipyramids and selenate tetrahedra.

Rapid Communication

An anion substitution route to low loss colossal dielectric $CaCu_3Ti_4O_{12}$
Andrew E. Smith, T.G. Calvarese, A.W. Sleight and M.A. Subramanian
Page 409

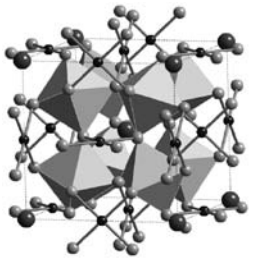

An anion substitution route was utilized for lowering the dielectric loss in $CaCu_3Ti_4O_{12}$ (CCTO) by partial replacement of oxygen by fluorine. This substitution, confirmed by fluorine analysis, reduced $\tan\delta$, and retained a high dielectric constant that was essentially temperature independent from 25 to 200 °C at 100 kHz.